Research Article Vol. 11, No. 9 / 1 Sep 2021 / Optical Materials Express 3154
Optical Materials EXPRESS

SERS fluctuations of NAD molecules adsorbed on arrays of Au nanocylinders

FILIPE B. MAGALHÃES,[1,3] RUTH F. V. V. JAIMES,[2,4] PAOLA CÓRIO,[2,5] AND WALTER J. SALCEDO[1,6]

[1]*Microelectronics Laboratory, Department of Electrical Engeneering, Polytechnic School, University of Sao Paulo, Av. Luciano Gualberto, tr3, Sao Paulo, Brazil*
[2]*Molecular Spectroscopy Laboratory, Chemistry Institute, University of Sao Paulo, Av. Lineu Prestes, 748, Sao Paulo, Brazil*
[3]*filipem@lme.usp.br*
[4]*rfvillam@iq.usp.br*
[5]*paola@iq.usp.br*
[6]*wsalcedo@lme.usp.br*

Abstract: Detection of a single molecule is a highly fluctuating event in surface-enhanced Raman scattering (SERS) measurements. Explaining these dynamic blinking events remains a challenge. To investigate this fluctuating behavior, we manufactured Au nanocylinder arrays. A monolayer of nicotinamide adenine dinucleotide (NAD) on the nanocylinder array exhibited intense and fluctuating Raman lines. Persistent Raman lines were not observed over time. These fluctuations were discussed within the dynamic back-action parametric interaction between the plasmon mode and vibrational modes. The results suggest that the highly efficient SERS structure promotes the formation and destruction of protuberances smaller than 2 nm at random on the nanocylinder surface.

1. Introduction

Surface-enhanced Raman scattering (SERS) has been widely studied [1–6]. The origin of this effect is attributed to the local evanescent electric field enhancement induced by localized resonant plasmon known as hot spot [5,6]. The excitation of these plasmons depends on the metals used, which are normally Au and Ag. The plasmons are excited because, within the visible spectral range, the real and imaginary parts of their dielectric permittivity of these metals have high negative and low values, respectively. [7,8]. Furthermore, plasmon excitation depends on the geometry of the nanoantennas. These geometries consist of spherical nanoparticles [9,10], nanoshells [11], nanorings [12], nanorods [13,14], nanostars [15,16] dimers [17,18], and particle oligomers [19,20]. Raman enhancement by this mechanism has shown high values of about ten orders of magnitude [5]. This large enhancement has potential for use in many applications, such as high-sensitivity analytical and bioanalytical detection systems also showing promising results in the intensification of catalytic effects [10–14,21,22].

The Raman enhancement sensitivity reaches the single-molecule level [10–12]. However, single-molecule detection by SERS is challenging. This is because it has been achieved only at high local electric field enhancements confined within a tiny spatial volume, which is of the order of the sub-nm^3 scale [13,14]. Highly efficient SERS structures for single-molecule detection require sophisticated fabrication processes. For example, dimer nanoantennas separated by a distance of only a few nanometers [18–20] or nanoparticle-on-mirror [23–26] have been reported.

Single-molecule events have been shown to be highly fluctuating phenomena [13–17]. Despite the well-controlled fabrication of SERS structures, the fluctuations in the SERS spectra have proved problematic for some applications. For example, problems can occur when these structures are applied to analytical systems for detecting molecular moieties [27,28]. The dynamics of the

#434894 https://doi.org/10.1364/OME.434894
Journal © 2021 Received 23 Jun 2021; revised 11 Aug 2021; accepted 19 Aug 2021; published 26 Aug 2021

Optical Materials EXPRESS

SERS fluctuation at room temperature depend on different uncontrolled variables. These variables include the nanoparticle structure, molecular structure, and interaction between nanoparticles and molecules. The interaction, in turn, may involve electron transfer, diffusion, change in the nanoparticle structure, or in the molecule structure [29,30]. In addition, the SERS fluctuation provides different opportunities for the study and analysis of the dynamics involved in this phenomenon. SERS fluctuations also depend on the structure of the molecules. Thus, simple molecules with few vibrational normal modes could promote different fluctuation events compared to molecules with a high number of vibrational normal modes.

In this study, nicotinamide adenine dinucleotide(NAD) was chosen as the target molecule because (i) it is a complex molecule with a high number of vibrational modes and (ii) it is essential in all biological systems. NAD consists of two nucleotides, ribose rings with adenine, and nicotinamide; a diphosphate bond keeps all these parts joined [31]. NAD exists in an oxidized (NAD^+) or reduced (NADH) form, which acts as a hydrogen acceptor or donor, respectively. Normally, the NAD redox reaction is catalyzed by enzymes. Inside cells, the fragile equilibrium of the intracellular redox state is maintained by the concentrations of oxidized and reduced forms of NAD [32–35]. Therefore, owing to its redox characteristics, NAD plays various roles in biological systems. NAD is a substrate, coenzyme, redox partner, neurotransmitter, and neuromodulator that participates in the post-translational modifications of proteins, signal transduction, regulation of energy metabolism, cell death, aging, extracellular cell-to-cell communications, transcription and gene expression, and DNA repair [36–45]. Under stress conditions, the levels of NAD in mitochondria also determine cell survival [46]. At mitochondrial cristae, NADH donates electrons that are used to synthesize adenosine triphosphate (ATP). ATP is used in the formation of human DNA phosphodiester bonds [47]. NAD also shows potential for use in many applications in medicine and in the drug industry. Some of these applications include anticancer, antibiotic, antiviral, immunosuppressant, rosacea atopic dermatitis, and Alzheimer's disease treatments [47–49]. Thus, studying NAD dynamics associated with redox reactions is important for understanding the metabolism of any biological system. The most important technique used to study the NAD dynamics related to its vibrational modes has been the SERS technique [50–52]. To the best of our knowledge, the majority of SERS results of NAD^+ published so far have not reported any fluctuation events.

In this paper, we report the fabrication of Au nanocylinder arrays through a one-step Au deposition process and two-step deposition process. For this purpose, organized porous alumina structures were used as masks. The nanoarray fabricated by two-step deposition showed a high SERS intensity for the Raman lines of NAD. This structure also showed fluctuation events that were similar to single-molecule events. The system was studied as a function of laser source excitation and laser power. The results indicated a highly uncorrelated event over time and over frequencies of NAD vibrational modes. These results were discussed in terms of the dynamic back-action parametric interaction between the plasmon mode and vibrational modes. The results suggest that the highly efficient SERS and fluctuation phenomena were induced by random protuberance formation and destruction on the nanocylinder surface. These protuberances would be smaller than 2 nm.

2. Materials and methods

Au nanocylinder arrays were obtained after the deposition of metal (Ti, Au) on a silicon substrate. This substrate was thermally oxidized so that a thin film of thermal silicon oxide (SiO_2) could form on its surface. Then, metal deposition was carried out on the SiO_2 surface to prevent direct contact between the metal structures and the Si substrate. The nanoarray features were obtained using ordered porous alumina as a mask.

First, Si with a type P (100) orientation and 10 Ω-cm were cleaned using a traditional microelectronic procedure. Second, the Si was oxidized in dry oxygen at 1150 °C, resulting

Optical Materials EXPRESS

in the formation of a thin SiO_2 film with a thickness of 75 nm. A porous alumina mask was attached to the SiO_2 surface. The oxide surface was made hydrophilic using the traditional microelectronic cleaning method. The cleaning consisted of immersion in a mixed solution of H_2SO_4 [98%]:H_2O_2 [38%] (3:1) at 105 °C for 1 h, followed by washing in deionized water. Then, the substrate was kept in a solution of H_2O:NH_4OH [36%]:H_2O_2 [38%] (5:1:1) at 75 °C for 15 min. Afterwards, the substrate was washed with deionized water several times, followed by drying under an N_2 gas jet.

The anodized aluminum oxide membranes (Topmembranes Co. Ltd.) were attached to the pre-treated SiO_2 surface according to the procedure indicated by the manufacturer of the porous alumina. Membranes with pore diameters of 30 nm, 60 nm, 80 nm, and 100 nm were used. Four cleaned acetone recipients were prepared, and then the membrane on the PMMA film and silicon substrate were held together using a clamp. The silicon substrate with the membrane was then partially immersed in the first acetone recipient for 30 min. In this step, the PMMA supporting substrate was dissolved, and the floating bare porous alumina film was attached to the Si/SiO_2 substrate. The substrate was dried at room temperature, rotated 180 degrees, and immersed again for another 30 min, followed by drying in the same way. Then, the Si substrate with the aluminum oxide membrane was dried and completely immersed in a second cleaned acetone recipient for 15 min, followed by drying at room temperature. This process was repeated for the third and fourth recipients. Finally, the stuck structure was immersed in isopropanol at 70 °C for 15 min. This step was introduced to eliminate acetone residues in the stuck structure. The samples were then completely dried under a vacuum. The aluminum oxide membrane stuck on the SiO_2 substrate served as a mask for obtaining an organized array of Au nanocylinders.

Metal deposition on the exposed areas (pores) was performed using the electron beam technique. The vacuum chamber was maintained at a pressure of 5.3×10^{-7} mBar during the deposition of 5 nm of Ti. The pressure was maintained at 6.1×10^{-7} mBar during the deposition of 20 nm of Au. An additional deposition of 2 nm of Au was made on the sample with a membrane with a pore diameter of 60 nm. Au thickness was monitored by a quartz cristal in the vacuum chamber during deposition. The role of titanium was to increase the adhesion between the gold and silicon oxide surfaces. In the final step, the alumina membrane was removed using a glue film, resulting in an Au nanocylinder array over the SiO_2 structure. Figure 1 shows a schematic of the Au nanocylinder array fabrication process.

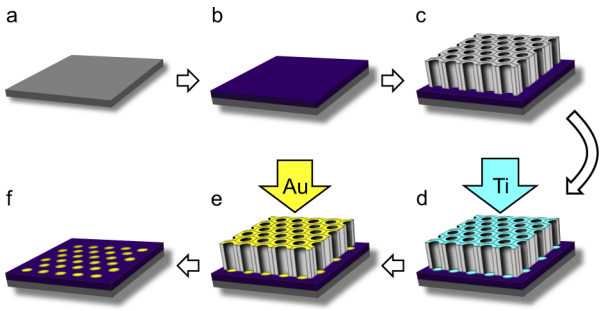

Fig. 1. Schematic of the process employed to prepare nanocylinders on the SiO_2 substrate. (a) cleaned Si, (b) thermally grown SiO_2, (c) membrane deposition, Ti, (d) membrane deposition, Au, (e) deposition by electron beam, and (f) nanocylinder organized after removal of the membrane.

The adsorption of NAD molecules on the Au nanocylinder arrays occurred through the following process: (i) A 10^{-3} M aqueous solution of NAD was prepared using NAD powder (Sigma Aldrich); (ii) the Au nanocylinder arrays (on Si/SiO_2 substrate) were immersed in this solution and incubated at room temperature for 24 h; and (iii) the samples were washed with

Optical Materials EXPRESS

distilled water to ensure the deposition of only one monolayer or less of the NAD molecules in order to observe the Raman intensification effect due to the localized plasmons. Thus, avoiding Raman scattering contributions from NAD molecules clusters which may have high-density NAD molecules; (iv) the samples were dried using an N_2 gas jet. The micro-Raman spectra of the samples were obtained using a Renishaw InVia-2000 Raman spectrometer. Laser sources of 532 nm, 633 nm, and 785 nm were used at different powers, as described in the results and discussion section. The laser beam was focused on the sample using an objective lens of 50× and an NA of 0.75. Raman spectra were acquired using the scan mode. Some samples without NAD were used for optical and structural characterization. Optical characterization was performed by the reflectance technique using the Ocean Optic USB-4000 spectrometer. Structural characterization was performed using scanning electron microscopy (SEM) Inspect-F50 FEI Co. The electron energy used was 20 kV in all the SEM images at different magnifications.

3. Results and discussion

3.1. Structural characterization of Au nanoarrays

Figures 2(a)—(e) depict the SEM images of the arrays of nanocylinders with diameters of 30 nm, 60 nm, 80 nm, and 100 nm.

Figures 2(a)—2(e) show that the metallic nanostructures have bidimensional compact hexagonal unitary cells. In addition, the unitary cells extend over the large surface area, even though some punctual defects can be observed in some samples. These results revealed that the porous alumina patterns were successfully transferred after Ti and Au deposition by the electron beam technique. As a result, Au nanocylinder periodic arrays were fabricated. From these SEM images, the geometrical parameters of the arrays were obtained. The results exhibited good correspondence with the nominal parameters provided by the porous alumina manufacturer (Table 1). The experimental parameters were used to obtain different theoretical results, such as the reflectance spectra and near-field enhancement of the arrays. These results were obtained using the Lumerical FDTD platform.

Table 1. Nominal parameters of the porous alumina mask used for gold nanoarrays fabrication and experimental parameters of the nanoarrays obtained.

Nominal pore diameter of the alumina mask	30 nm	60 nm	80 nm	100 nm
Effective diameter of the Au nanoarrays	30 nm ± 2.9 nm	63 nm ± 5	78 ± 10 nm	98 ± 7 nm
Nominal pore periods in the alumina mask	65 nm	125 nm	100 nm	125 nm

3.2. Optical reflectance characterization

Figure 3(a) shows the reflectance spectra of the arrays corresponding to nanocylinder samples with diameters of 30 nm, 60 nm, 80 nm, and 100 nm. The 80 nm and 100 nm arrays showed almost the same minimum of approximately 500 nm; for the 30 and 60 nm samples, the minimum redshifted. This minimum reflectance is related to the plasmon polaron grating behavior of the sample. The theoretical spectra follow the same trend, as shown in Fig. 3(b). However, in the 700 nm region , the experimental spectra of the 80 nm and 100 nm samples diverged from the theoretical spectra. These differences could be attributed to the different techniques used to obtain the experimental and theoretical spectra: the experimental results were obtained with diffuse reflectance techniques, whereas the theoretical reflectance was obtained using a specular setup. Hence, no scattering effect was considered in the theoretical results. In Figs. 3(a)—(b), all experimental and theoretical spectra indicate the grating feature of all the sample arrays.

Optical Materials EXPRESS

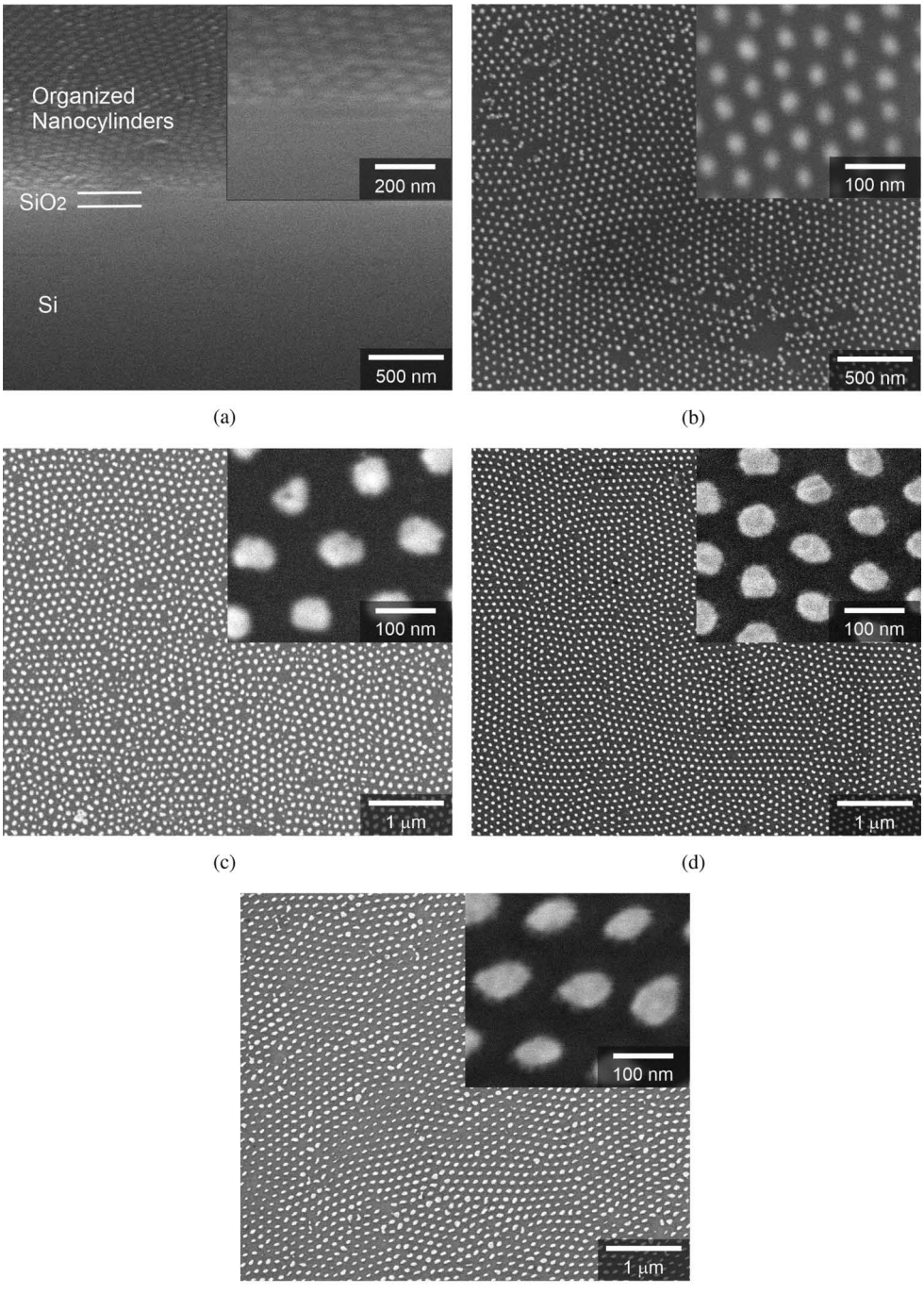

Fig. 2. SEM characterization of the nanocylinders. (**a**) Nanostructure perspective image at 20° showing the organized nanocylinders, SiO_2 layer, and Si substrate. (**b—e**) Top views of the organized nanocylinders with diameters and periodicities of (**b**) 30 nm and 65 nm, (**c**) 60 nm and 125 nm, (**d**) 80 nm and 100 nm, and (**e**) 100 nm and 125 nm, respectively.

Optical Materials EXPRESS

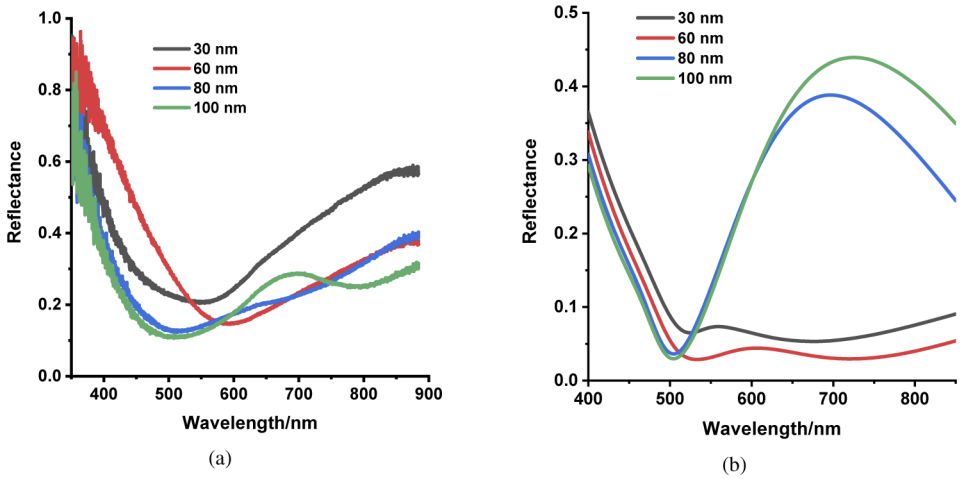

Fig. 3. (**a**) Experimental Reflectance spectra of nanocylinder arrays with diameters of 30 nm, 60 nm, 80 nm, and 100 nm. (**b**) Theoretical reflectance spectra obtained using the experimental parameters from SEM images. These spectra were calculated by using Lumerical FDTD (finite-difference time-domain) platform

3.3. Raman spectra

3.3.1. Raman spectra as a function of the excitation laser and array structures

As described in the experimental procedure, the samples were rinsed with distilled water after immersion in the NAD solution. We ensured that only a monolayer of NAD molecules remained adsorbed on the sample surfaces. SERS spectra corresponding to arrays of 30, 60, 80, and 100 nm (diameter of nanocylinders) were obtained. The spectra were obtained after excitation with a 785 nm laser light at a constant power of 3.5 mW.

It is well known that NAD molecules exhibit a high number of active Raman modes that can also depend on the oxidation state of NAD [50–54]. The powdered NAD exhibited some principal Raman lines (Supplement 1): the line at 730 cm^{-1} corresponds to the stretching mode of the adenine ring [49–53]; the line at 1030 cm^{-1} is related to a nicotinamide ring vibration [50–54]; the line at 1113 cm^{-1} is related to the vibration of the ribose close to the nicotinamide part; the line at 1324 cm^{-1} is related to the adenine ring vibration or to the NH_2 rock mode; the line at 1407 cm^{-1} is related to the adenine ring vibration; and the line at 1510 cm^{-1} is also related to another vibration mode of the adenine ring [50–54]. In the powdered NAD, the 1030 cm^{-1} Raman line showed the highest intensity, followed by the line at 730 cm^{-1}. This indicates that the Raman cross section of the nicotinamide ring vibration has the highest value for NAD molecules. From the SERS spectra depicted in Fig. 4(a), the Raman enhancement is related to the structural features of the arrays. The arrays of nanocylinders with diameters of 30, 80, and 100 nm showed very low Raman intensities for some vibrational modes of NAD. The samples with diameters of 80 and 100 nm showed a low Raman line at 736 cm^{-1}, corresponding to the stretching mode of the adenine ring vibration. This suggests that NAD molecules are preferentially adsorbed throughout the adenine moiety in these samples. The sample with a nanocyclinder diameter of 30 nm showed an extremely low Raman line at 1490 cm^{-1}, which is also related to the adenine ring vibration, as mentioned above. Note that a smooth thin film of Au was used as a reference (with the same thickness and composition as the nanocylinder). In this study, no Raman lines of NAD were observed. Therefore, the low-intensity Raman lines for the samples with diameters of 30, 80, and 100 nm are effectively related to SERS phenomena. The broad Raman band (932

Optical Materials EXPRESS

cm^{-1} – 990 cm^{-1}) in this sample corresponds to the second-order transverse optical (TO) phonon of Si. This band was expected because the Au nanostructures were fabricated on the Si substrate.

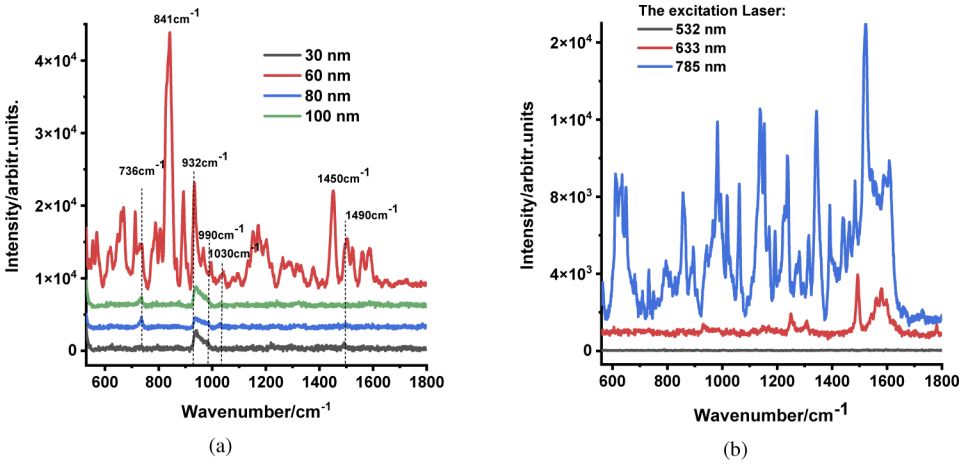

Fig. 4. (**a**) SERS spectra of NAD on the surface of arrays of nanocylinders with diameters of 30 nm, 60 nm, 80 nm, and 100 nm. The SERS spectra were obtained after excitation with a 785 nm laser having a power of 3.5 mW. (**b**) SERS spectra of NAD molecules on a nanocylinder array with a nanocylinder diameter of 60 nm excited with laser sources of 532 nm, 633 nm, and 785 nm.

In Fig. 4(a), the SERS spectrum of NAD on the sample with a diameter of 60 nm showed high-intensity Raman lines. One of the highest values at 841 cm^{-1} corresponds to the phosphate vibrational mode near the adenine of the NAD molecule. This line did not appear for the NAD powder sample or the arrays of nanocylinders with diameters of 30, 80, and 100 nm. In contrast, the Raman lines for the array with nanocylinders with a diameter of 60 nm fluctuated continuously. The origin of these fluctuations is discussed in Section 3.3.2. A rough estimate of the SERS enhancement for 841 cm^{-1} in the sample with a diameter of 60 nm is approximately four orders of magnitude. This enhancement level has been reported in the SERS of single-molecule detection [5]. As the 60 nm array showed high SERS intensities, SERS was studied as a function of laser excitation [Fig. 4(b)]. The results revealed that more efficient SERS was achieved using the 785 nm laser source. Although a significant enhancement was also observed at 633 nm, a considerably lower intensity was observed for those excited at 785 nm. No Raman line was observed with 532 nm laser excitation. The origin of the SERS behavior in relation to the array feature and the energy of the laser source is discussed in Section 3.3.2. This discussion is supported by theoretical calculations of the electric near-field behavior of these samples.

The near-field intensities of the nanocylinder arrays were calculated using Lumerical FDTD software. The geometrical parameters of the arrays obtained from the SEM images were used in this calculation. The near-field behavior creates the plasmon characteristic observed in the samples. Figure 5(a) depicts the calculated electric near-field intensity of the different arrays. In this figure, the behavior of the near field was first analyzed in the 785 nm region. At a wavelength of 785 nm, the sample corresponding to the array with nanocylinders having a diameter of 60 nm exhibited the highest enhancement. The same trend was observed in the experimental results of SERS, with the highest Raman intensities being observed for the sample with array of nanocylinders with a 60 nm diameter. The analysis results of the near-field spectrum of the array of nanocylinders with a 60 nm diameter [red curve in Fig. 5(a,)] revealed that the 785 nm excitation resulted in the highest enhancement, followed by the 633 nm and 532 nm excitations.

Optical Materials EXPRESS

These trends were also observed in the Raman spectra of NAD in the array of nanocylinders with a 60 nm diameter [Fig. 4(b)].

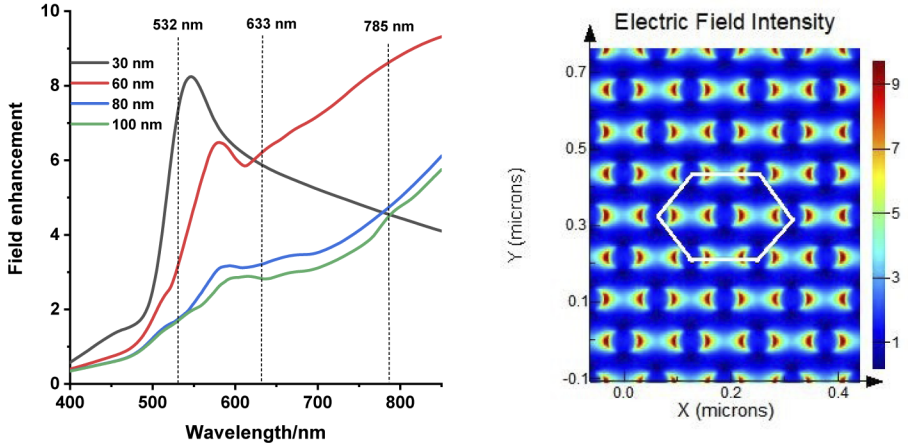

(a) (b)

Fig. 5. (**a**) Near electric field intensity spectra of the arrays of nanocylinders with diameters of 30, 60, 80, and 100 nm. The vertical dashed line indicates the location of the laser sources used to excite the experimental sample. (**b**) Image of the near-field intensity at 785 nm corresponding to the array of nanocylinders with a diameter of 60 nm. The scale of the color bar corresponds to the relative intensity of the electric near field in relation to the intensity of the incident electric field, which in the simulator is considered as a unit value.

The near-field feature of the array of nanocylinders with a 60 nm diameter at 785 nm revealed the local plasmon dipole responsible for near-field enhancement. Consequently, this local plasmon was also responsible for the SERS enhancement in the experimental results. The FDTD calculation explains the trends of the experimental SERS results in relation to the array structures and laser source excitation. However, the theoretical low-field enhancement cannot successfully explain the large SERS intensities observed in the samples, especially in the array of nanocylinders with a 60 nm diameter. According to the conventional mechanism of the electromagnetic origin of SERS, Raman enhancement should occur E^4/E_0^4 [55]. In our calculation, E^4/E_0^4 achieved a maximum enhancement of 64 times. In turn, the Raman lines of NAD molecules on the sample consisting of nanocylinders with a 60 nm diameter fluctuated over time under the same experimental conditions. This behavior cannot be explained by the conventional electromagnetic mechanism of the local plasmons. In Section 3.3.2, the high SERS effect and fluctuation of the Raman lines of NAD on the array of nanocylinders with a 60 nm diameter are discussed. We suggest a possible mechanism for these effects.

3.3.2. SERS fluctuation

As described above, the SERS of NAD adsorbed by the 60 nm array showed an extraordinary enhancement effect. The enhancement was approximately 6.5×10^4 times for some vibrational modes when the sample was excited with a 785 nm laser source. For example, Fig. 8 shows the vibrational mode at 1464 cm^{-1} corresponding to the ribose vibration part near the nicotinamide moiety in the NAD molecule. In addition to being very intense, the Raman line of this sample also fluctuated over time. In addition, the fluctuation pattern depended on the power of the laser excitation. Raman fluctuations were observed when the experimental setup was adjusted to detect a single molecule [56]. As the absorption of NAD in our sample is practically a monolayer,

Optical Materials EXPRESS

SERS fluctuation could be considered a single-molecule event. Further details about this event will be given in this section.

To study the dynamic behavior of these fluctuations, the Raman spectra in the scan mode and each scan time (T) were recorded. In all cases, T had a duration of 20 s (i.e., a new Raman scan was recorded every 20 s). NAD spectra were obtained by a 60 nm array using a 785 nm excitation laser source. Figures 6–10 depict the Raman spectra of NAD in the array of nanocylinders with a diameter of 60 nm excited with a 785 nm laser source. In Figs. 6–10, the powers of the laser source are 7 mW, 3.5 mW, 700 μW, 350 μW, 35μW, and 70 nW, respectively. Additionally, the bidimensional maps of these spectra were depicted considering three level scales defined at the maximum Raman peak (I_max), $I_max/2$, and $I_max/4$. In each of the image maps, a low threshold level was considered, which was above the noise level of the Raman signal. Thus, the images avoid noise signals.

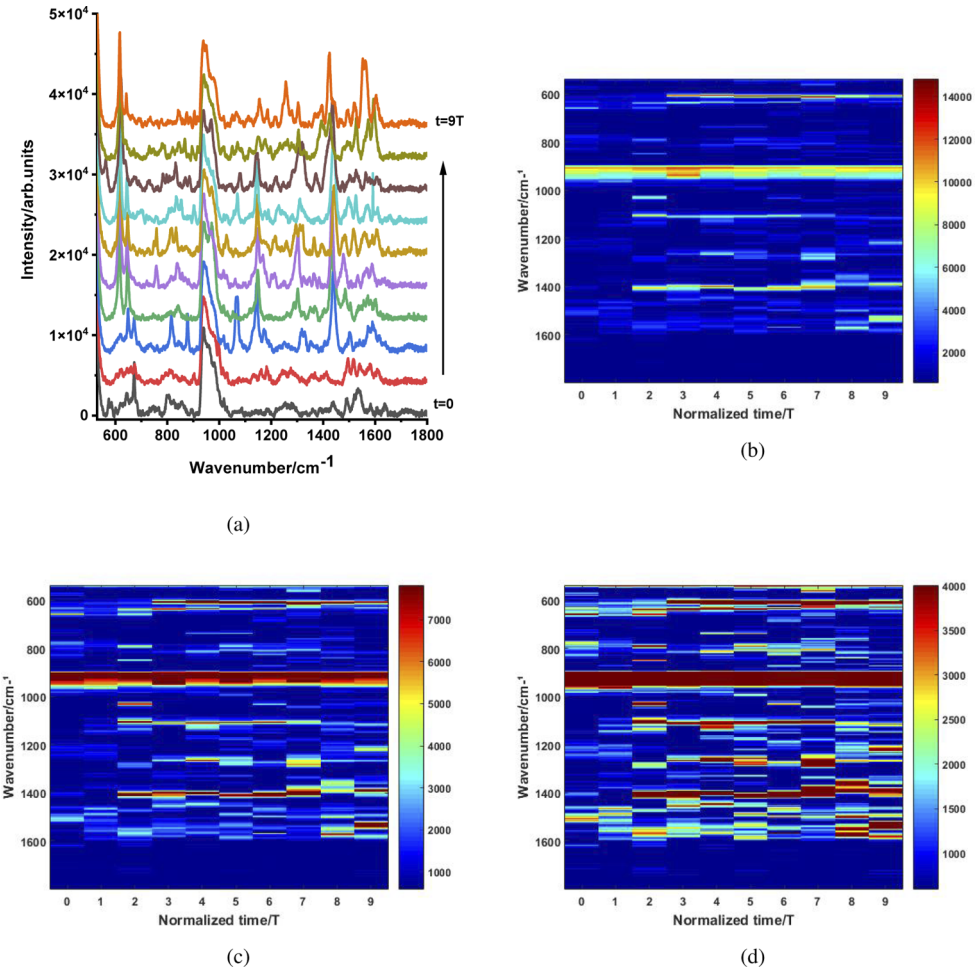

Fig. 6. SERS spectra of a NAD molecule on the array of nanocylinders with a diameter of 60 nm excited with a 785 nm laser source at a power of 7 mW. (**a**) Spectra correspond to the corrected background. (**b**) 2D map image of SERS spectra using the highest peak intensity scale. (**c**) 2D map image of SERS spectra using half of the highest peak intensity scale. (**d**) 2D map image of the SERS spectra using a quarter of the highest peak intensity scale. In each image, low-level thresholds are defined above the signal noise level . Therefore, the images represent only Raman signals.

Optical Materials EXPRESS

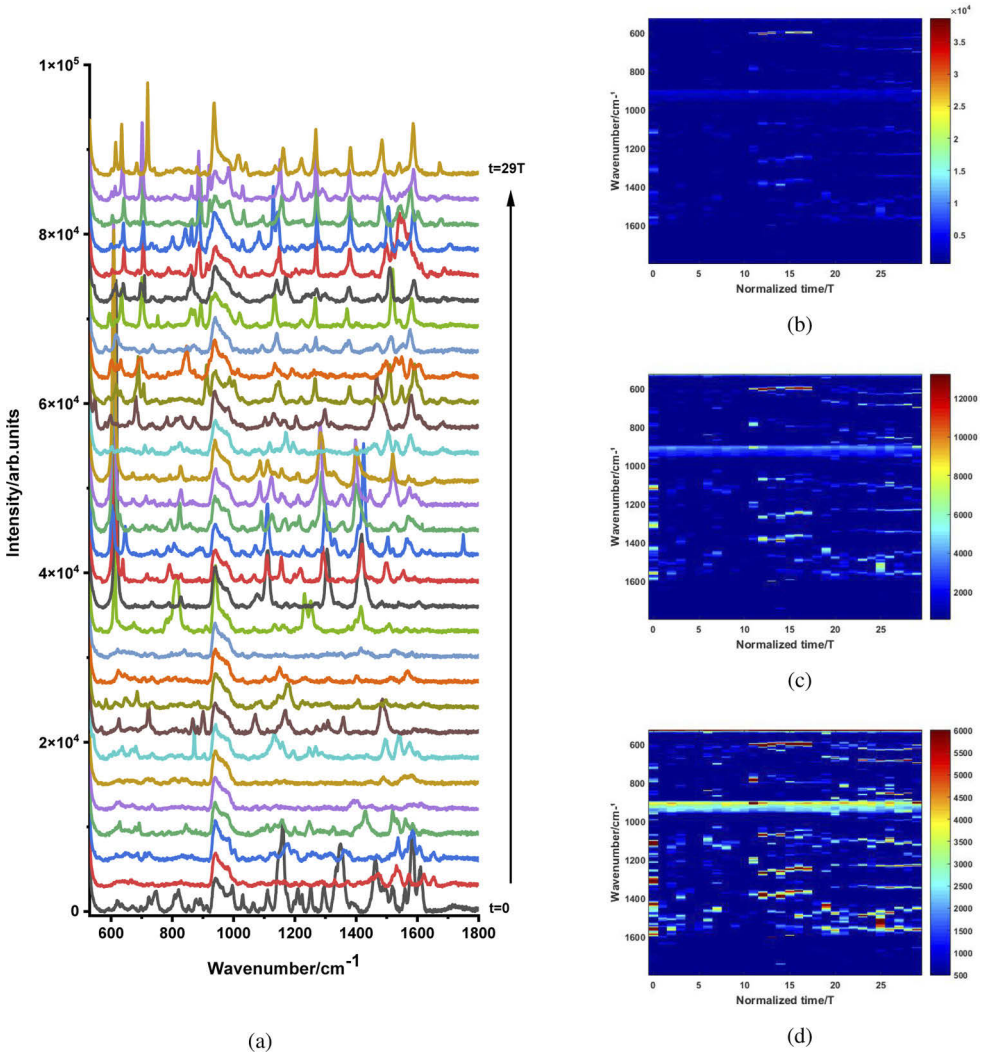

Fig. 7. SERS spectra of a NAD molecule on the array of nanocylinders with a diameter of 60 nm excited with a 785 nm laser source at a power 3.5 mW. (**a**) Spectra correspond to the corrected background. (**b**) 2D map image of SERS spectra using the highest peak intensity scale. (**c**) 2D map image of SERS spectra using half of the highest peak intensity scale. (**d**) 2D map image of the SERS spectra using a quarter of the highest peak intensity scale. In all images, the low-level threshold was defined above the noise level of the signal. Therefore, the images represent only Raman signals.

When the power excitation was 7 mW [Figs. 6(a)—6(b)], the highest Raman line was located at 618 cm^{-1}. This Raman line was assigned to adenine vibration and had an intensity 1.3 times larger than that of the second order of the TO phonon of silicon. At a power of 7 mW, the second-order TO phonon Raman spectrum of Si was intense and constant over time. The Raman line at 1432 cm^{-1} related to ribose vibration was also intense compared with other Raman lines. Even though these lines were intense, they fluctuated over time. The fluctuation of other Raman lines [Fig. 6(c)] was more frequent over time, with a slight shift in the mode oscillation frequency.

Figures 7(a)—7(c) show the Raman spectra and their 2D map representation when the excitation laser power was 3.5 mW. Here, the most intense Raman line was placed at 619 cm^{-1} (vibration

Optical Materials EXPRESS

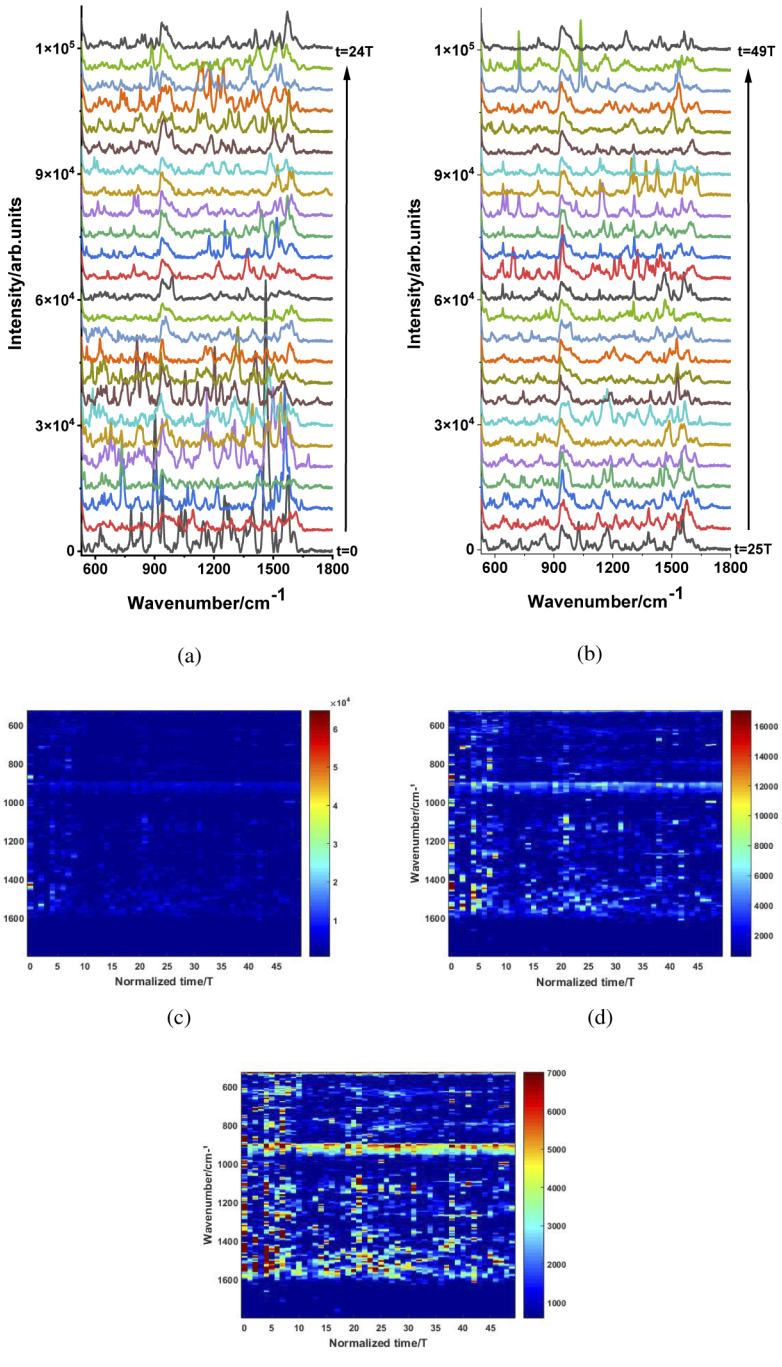

Fig. 8. SERS spectra of a NAD molecule on the array of nanocylinders with a diameter of 60 nm excited with a 785 nm laser source at a power of 700 μW. (**a**) and (**b**) spectra correspond to the corrected background. (**c**) 2D map image of SERS spectra using the highest peak intensity scale. (**d**) 2D map image of the SERS spectra using half of the highest peak intensity scale. (**e**) 2D map image of the SERS spectra using a quarter of the highest peak intensity scale. In all images, the low-level threshold was defined above the noise level of the signal. Therefore, the images represent only Raman signals.

Optical Materials EXPRESS

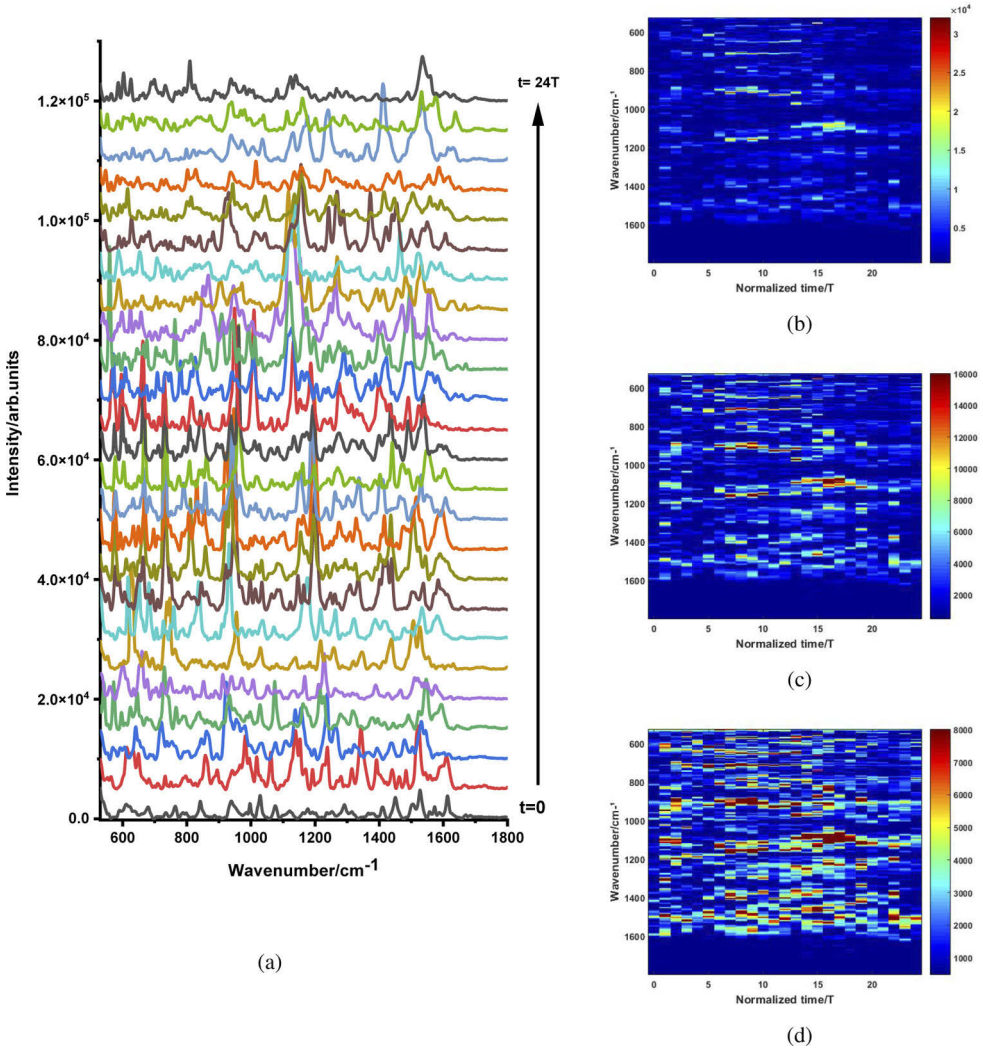

Fig. 9. SERS spectra of a NAD molecule on the array of nanocylinders with a diameter of 60 nm excited with a 785 nm laser source at a power of 350 μW. (**a**) Spectra correspond to the corrected background. (**b**) 2D map image of SERS spectra using the highest peak intensity scale. (**c**) 2D map image of SERS spectra using half of the highest peak intensity scale. (**d**) 2D map image of the SERS spectra using a quarter of the highest peak intensity scale. In all images, a low-level threshold was defined above the noise level of the signal. Therefore, the images represent only Raman signals.

Optical Materials EXPRESS

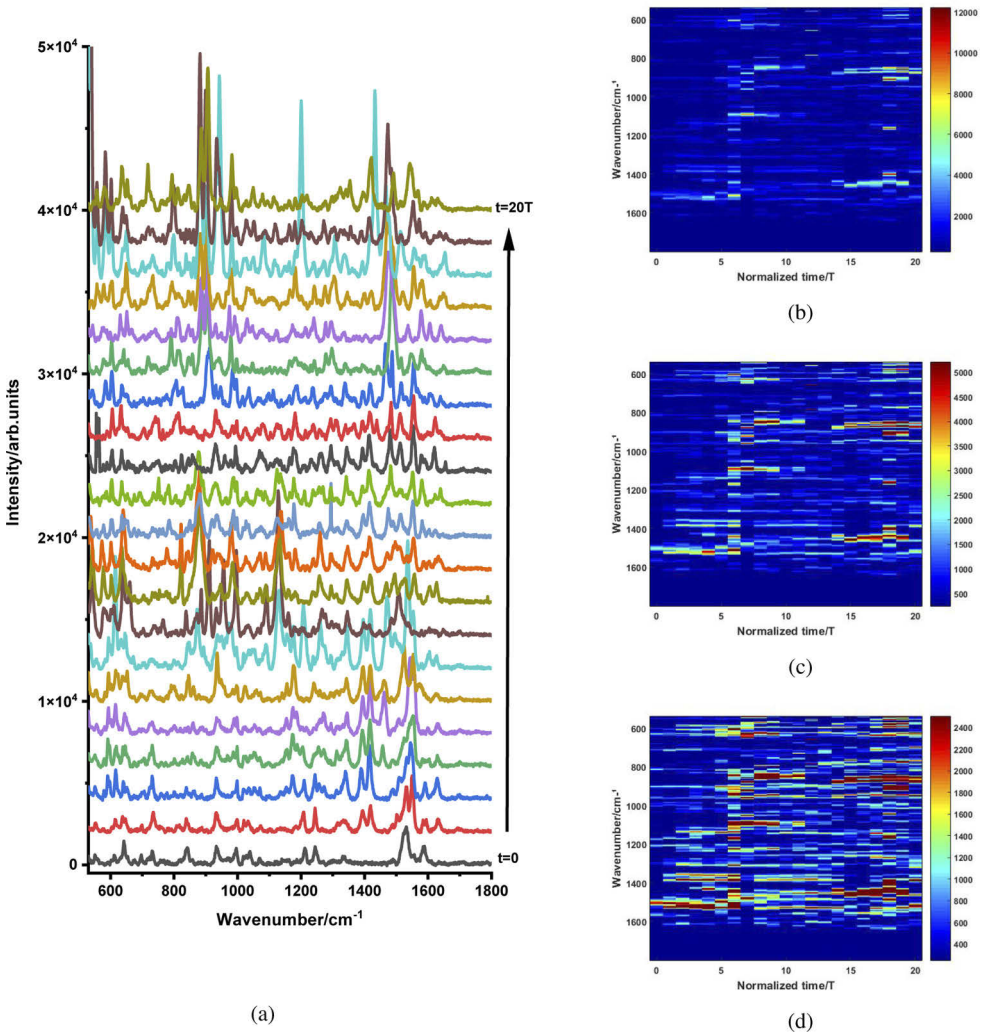

Fig. 10. SERS spectra of a NAD molecule on the nanocylinder array with a diameter of 60 nm excited with a 785 nm laser source and 35 μW of power. (**a**) Spectra correspond to the corrected background. (**b**) 2D map image of SERS spectra using the highest peak intensity scale. (**c**) 2D map image of SERS spectra using half of the highest peak intensity scale. (**d**) 2D map image of the SERS spectra using a quarter of the highest peak intensity scale. In all images, a low-level threshold was defined above the noise level of the signal. Therefore, the images represent only Raman signals.

Optical Materials EXPRESS

mode of adenine). Its intensity was 5.5 times that of the second-order TO phonon Raman of Si. A lower Raman intensity of Si was expected because a low power laser was used. However, the intensity of the most intense Raman line of NAD increased in relation to the Si Raman line, which was assumed to be an internal reference. Even though the Raman line at 619 cm^{-1} showed the highest intensity line, this line fluctuated over time and exhibited a blinking behavior [Fig. 7(b)]. Other lower-intensity Raman lines [Figs. 7(c) and 7(d)] fluctuated over time in a more random manner compared to those for the 7 mW power laser. Additionally, the fluctuation was observed to promote the appearance of new vibration modes because this fluctuation also occurred in the vibration frequencies of NAD. For a laser power of 700 μW [Figs. 8(a)–8(d)], the highest Raman line appeared on the first recording scan and disappeared on other scans (Fig. 8(a)). This Raman line was located at 1464 cm^{-1} and was related to the ribose vibrational mode [50–54]. The line had an intensity that was approximately 19 times that of the second-order TO phonon intensity of Si. As expected, the Si Raman band decreased owing to the lower power of the laser. In contrast, the SERS effect remained intense. Other less intense Raman lines showed random fluctuations over time at other vibrational frequencies [Fig. 8(c)—8(d)].

For a laser power of 350 μW [Figs. 9(a)—9(d)], the second-order Si Raman band practically disappeared. In addition, three Raman lines of NAD appeared at different recording times. These lines had high intensities on the order of 3×10^4 (arbitrary units). They occurred at 728 cm^{-1}, 949 cm^{-1}, and 1197 cm^{-1}. The lines are related to the vibrational modes of the adenine ring, nicotinamide, and ribose, respectively [50–54]. As before, the low-intensity Raman lines fluctuated randomly over time in other frequency vibration modes. For a laser power of 35 μW (Fig. 10), there were four Raman lines with approximately the same intensity (highest) of the order of 1.3×10^4. These Raman lines appeared at different recording times and disappeared over time [Figs. 10(a)—10(b)]. Again, the less intense Raman lines fluctuated randomly over time at other vibrational frequencies [Figs. 10(c) and 10(d)]. Surprisingly, the fluctuated Raman lines [Figs. 11(a)—11(c)] were also observed for the 70 nW power laser. In this experiment, the highest Raman line, which was related to phosphate or nicotinamide vibration, appeared at 921 cm^{-1}, [50–54]. Moreover, another intense Raman line was occurred at 704 cm^{-1}, corresponding to the adenine ring vibration [50–54]. At this power, the fluctuation over time and the frequencies of the vibration modes were random.

Note that all the lines fluctuated such that there was no persistent Raman vibrational mode. Thus, each Raman line recorded in one scan did not appear again in the subsequent recording scan. These behaviors are more evident for Raman spectra excited with a laser power equal to or less than 3.5 mW. This indicates a more random fluctuation behavior for the low-power excitation laser. The non-existence of persistent Raman lines in our experiment differs from the results reported in [57,58], where some persistent Raman lines were identified and other Raman lines with blinking behavior.

To quantify the random SERS fluctuation, the concept of a co-occurrence matrix was used. The co-occurrence matrix is widely used for the texture analysis of images [59]. The gray-level co-occurrence matrix (GLCM) characterizes the texture of gray-level images through contrast, dissimilarity, homogeneity, energy, entropy, mean, variance, and correlation parameters [59–61]. As we were interested in the Raman line fluctuation over time and the vibration mode frequencies, we determined the correlation parameter over time and the vibrational mode frequencies. Therefore, the set of Raman spectra as a function of time and wavenumber was used as a grayscale image matrix. The GLCM correlation parameters were obtained using Eqs. (1)–(3). [59–61]:

GLCM mean [Eq. (1)]:

$$\mu = \sum_{i=0}^{N_g-1} \sum_{j=0}^{N_g-1} iP(i,j) \tag{1}$$

Optical Materials EXPRESS

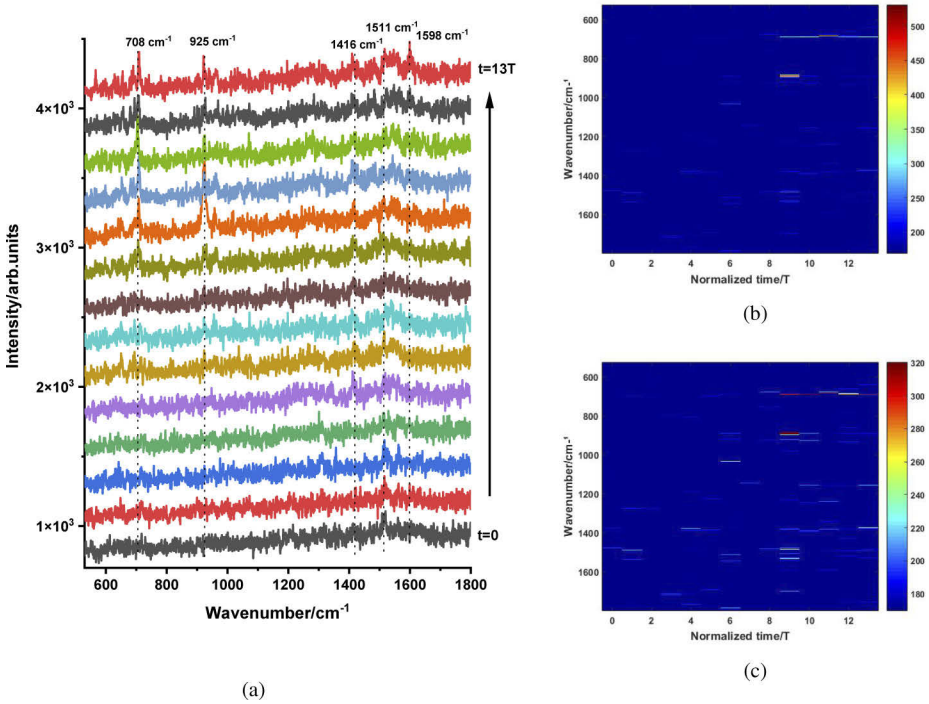

Fig. 11. (**a**) SERS spectra of the NAD molecule on the array of nanocylinders with a diameter of 60 nm excited with a 785 nm laser source at a power of 70 nW. (**b**) 2D map image of SERS spectra using the highest peak intensity scale. (**c**) 2D map image of SERS spectra using half of the highest peak intensity scale. In all images, a low-level threshold was defined above the noise level of the signal. Therefore, the images represent only Raman signals.

GLCM variance [Eq. (2)]:

$$\sigma^2 = \sum_{i=0}^{N_g-1} \sum_{j=0}^{N_g-1} (i-\mu)^2 P(i,j) \tag{2}$$

GLCM correlation [Eq. (3)]:

$$C = \frac{\sum_{i=0}^{N_g-1} \sum_{j=0}^{N_g-1} (i-\mu)(j-\mu) P^2(i,j)}{\sigma^2} \tag{3}$$

where N_g is the number of gray levels. P(i,j) = P(i,j;d)is the normalized frequency with which two neighboring resolution cells separated by distance d occur in the image; one of the cells has gray tone i and the other has gray tone j. In the present study, d was related to the time distance when the correlation over time was determined. This distance corresponded to the time of resolution of the Raman spectrometer when determining the correlation over the wavenumber of the vibrational frequency modes.

The GLCM tools of the MATLAB R2015a platform were used to determine the correlations over time and the wavenumber offset. For this task, the value of N_g = 200 was defined because values greater than this did not have significant effects on the final results. Note that the gray level threshold was considered to be above the noise signal level of the Raman spectra. Thus, we

Optical Materials EXPRESS

ensured that the determined correlation values corresponded only to the Raman band intensities. Figures 12(a) and 12(b) show the correlation of the Raman spectra fluctuation over time and the wavenumber offset, respectively.

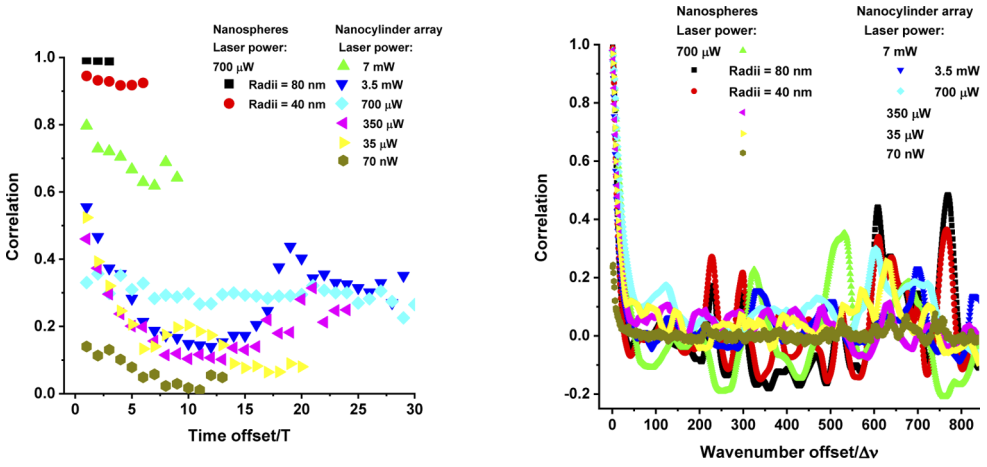

(a) (b)

Fig. 12. GLCM correlation coefficient as a function of (**a**) time offset and (**b**) wavenumber offset. Here, the minimum temporal distance was T = 20 s. T is the duration of one Raman spectrum acquisition recording scan. The minimum wavenumber distance is $\Delta\nu = 1\ cm^{-1}$, which corresponds to the Raman spectrometer resolution.

For comparative purposes, the SERS spectra of NAD were obtained by clustering gold nanospheres with diameters of 80 nm and 40 nm. The SEM images and Raman spectra of these SERS surfaces are depicted in Figs. S2–S5 in the supplementary material. In both cases, the Raman spectra showed the highest Raman line at 730 cm^{-1}, which corresponds to the adenine ring vibration, showing persistence over time. The SERS spectra of the 80 nm spheres did not show fluctuations in their different Raman lines. Some of the Raman lines of the SERS spectra from the cluster of 40 nm spheres slightly fluctuated.

In Fig. 12(a), the correlation over time of the SERS spectra from the cluster structure of 80 nm nanospheres is close to 1. For the cluster of 40 nm nanospheres, this correlation is approximately 0.93, which is almost constant over the offset time. For the sample of the 60 nm nanocylinder, the correlation over time depends on the laser power [Fig. 12(a)]. As described earlier, this sample has a highly fluctuating SERS structure. There is a high-level correlation (0.8 to 0.6) for a power of 7 mW. Then, the values decrease as the excitation power laser decreases to a level close to zero at a power of 70 nW.

The correlations as a function of the wavenumber offset showed high values near the zero offset. This was expected because each Raman band had a finite width. However, at offset distances greater than the Raman band width (20 cm^{-1}), the correlation decreased to approximately zero. Here, the offset distance was directly related to the separation spectral distance between the different Raman bands. The correlation for the 40 nm and 80 nm nanospheres showed an oscillating characteristic with some positive peaks. These peaks occurred at distances of 229, 299, 608, and 765 cm^{-1}, and were perfectly related to the Raman bands at these distances. For example, the peak correlations at 229 and 299 cm^{-1} agree with the separation distance between the Raman peaks at 736 cm^{-1} and 963 cm^{-1} and between 736 cm^{-1} and 1028 cm^{-1}, respectively (Figs. S4 and S5).

Optical Materials EXPRESS

Negative correlation or anticorrelation peaks exhibit opposite behaviors in the evolution of their intensities, that is, while one grows in intensity, the other decreases. Hence, if one band increases, the other decreases. An example is the first anticorrelation peak that occurred at 270 cm^{-1}. This peak agrees with the correlation behavior between the Raman lines at 963 cm^{-1} and 1237 cm^{-1}, which are separated by 274 cm^{-1} (see Figs. S4 and S5). This oscillating behavior of the correlation coefficient agrees with the high-value correlation over time offset (Fig. 8(a)). In the case of the nanocylinder array, the correlation coefficient showed oscillating behavior when the power of the excitation laser was 7 mW. The correlation approached zero at lower power values, which also corresponded well with the behavior of the correlation over time.

The Raman line fluctuations in our sample were strong random events. Therefore, the fluctuation did not only happen for certain well identified Raman lines, as observed by Carnegie et al. and Benz et al. [57,58]. In contrast, our results revealed that new Raman lines appeared at each new recording scan.

At this point, the strong random fluctuation could have been due to the existence of different vibrational modes in the NAD molecules. Under normal conditions, some of them are only infrared active, while others are only Raman active [54]. However, at a high intensity near the field originating from plasmon excitation, these rules can be broken. Therefore, the modes that were only active infrared can become Raman active as well [58]. All the principal Raman lines of NAD identified in the fluctuated SERS results are reported in the supplementary material in Table S1. Some Raman lines that have not been reported in the literature were observed in our work.

The origin of the high-intensity SERS effect and fluctuations in time are still controversial [57–62]. A more plausible explanation for this single molecular event is the formation of picocavities in plasmonic nanoparticles. These picocavities can spontaneously form and spontaneously destroy the nanoparticle surface at room temperature, resulting in a SERS fluctuation event [56,57].

A possible mechanism for the formation of the SERS fluctuation event is the spontaneous formation and/or spontaneous destruction of picocavities. To investigate this mechanism, the near-field intensity in the nanocylinder array was calculated. For this task, we used the Lumerical FDTD platform. Furthermore, we considered that the nanocylinders contain a small spherical protuberance of 2 nm radii (see Fig. 13).

Figure 13(a) shows two spectra of the electric near-field intensity (induced by plasmon excitation) of an array of Au nanocylinders with and without protuberances. The black line corresponds to the array with a protuberance at the edge of the Au nanocylinder. The red line corresponds to nanocylinders without protuberances. The field enhancement is dimensionless, because it is relative to the excitation light. The maximum near-field intensity of the array without protuberances was approximately 8 and had a large width band (see also Fig. 5(a)). Furthermore, the array containing a spherical shape with a 2 nm radii originated from a high-level band.

Nanocylinders with protuberances showed an intensity of approximately 340 at 796 nm and a width of approximately 30 nm. This gives a quality factor of the plasmon band of approximately Q = 27. This value was considered to be high in the plasmonic area. This value is comparable to the quality factor of an optical cavity, such as the Fabry–Perot cavity [63]. This plasmon is also strongly space-localized, as shown in Fig. 13(b). Note that spectral features, such as the position, width, and intensity of this plasmon band, depend on the diameter and periodicity of the nanocylinder. This is demonstrated in the theoretical calculation of the near-field spectra for all structures used in this study (see Fig. S6 in Supplement 1).

As mentioned above, the peak of the spectrum for the 60 nm nanocylinder array with protuberances (Fig. 13(a)) occurred at λ_p = 796 nm. The excitation laser used in the Raman fluctuation assay was λ_L = 785 nm. Therefore, the excitation light source is blue-shifted in relation to the plasmon energy, and the energy distance between 785 nm and 796 nm is approximately

Optical Materials EXPRESS

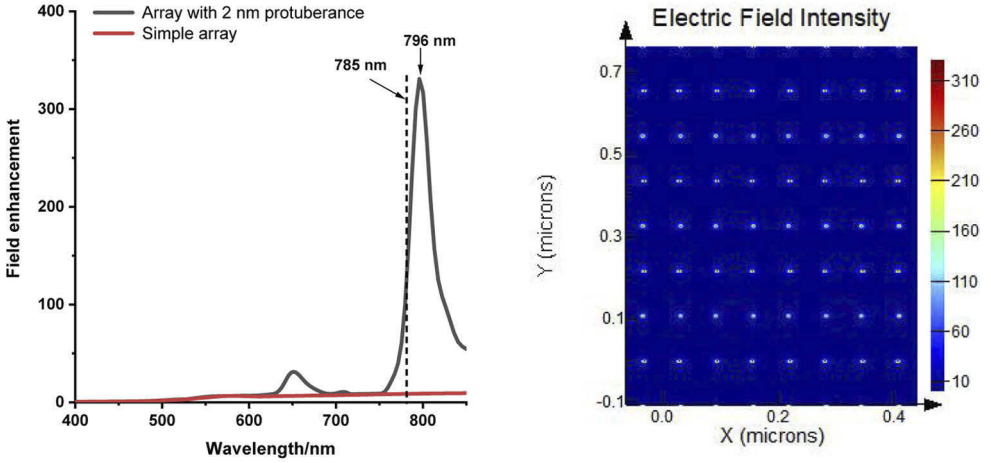

(a) (b)

Fig. 13. (**a**) Electric near field intensity of the array of Au nanocylinders with a diameter of 60 nm with a spherical protuberance of 2 nm radii (black line). Near-field intensity of a simple array of Au nanocylinders (red line). (**b**) Images of the near-field intensity of the array with a protuberance at 796 nm, which is the peak position of the black line spectrum in (**a**).

1620 cm^{-1}. The width of the plasmon band was approximately 2923 cm^{-1} ($\Delta\lambda$ = 30 nm). Thus, the spectral range of the Stokes Raman spectra of NAD molecules (530 cm^{-1} to 1800 cm^{-1}) was within the plasmon band. This is illustrated in Fig. S7 of Supplementary Material. If these conditions are satisfied, the high SERS enhancement in the sample could be explained by the dynamical back-action enhancement mechanism [2,63–65]. In this model, the plasmon cavity and vibrational modes of the molecules were considered opto-mechanical systems. Hence, the coupling between vibrational and plasmonic modes was considered a parametric interaction [2,57,64,65].

In our case, the plasmon cavities were an Au array with tiny protuberances. The total Hamiltonian of this system was expressed as $H = H_c + H_v + H_{int} + H_L$, where H_c and H_v are the plasmonic cavity Hamiltonian and molecular vibrational Hamiltonian, respectively, H_L is the incident (excitation) light Hamiltonian, and H_{int} is the coherent Hamiltonian interaction between the plasmonic modes and molecular vibrational modes [2,64,65]. Equations (4), (5), (6), and (7) define the terms H_c, H_v, H_{int}, and H_L, respectively.

$$H_C = \omega_C \hbar \hat{a}\hat{a}^+ \tag{4}$$

$$H_v = \omega_v \hbar \hat{b}\hat{b}^+ \tag{5}$$

$$H_{int} = g\hbar \hat{a}\hat{a}^+(\hat{b} + \hat{b}^+) \tag{6}$$

$$H_L = iE[\hat{a}_L^+ exp(-i\omega_L t) - \hat{a}_L exp(i\omega_L t)] \tag{7}$$

Here, $\hat{a}$, $\hat{a}^+$, $\hat{b}$, and $\hat{b}^+$ are bosonic creation and annihilation operators, respectively, and g is the opto-mechanical parameter that depends on the plasmon cavity frequency and the Raman polarizability of the molecule [2,64,65]. The Langevin equations can be used to determine the time evolution of $\hat{a}$ and $\hat{b}$, from which the Stokes and anti-Stokes photon populations are obtained [2,64,65]. Hence, the dynamic back action can be synthesized as follows: First, the molecular vibration acts on the resonance behavior of the plasmonic cavity such that the

Optical Materials EXPRESS

plasmon cavity resonance frequency exhibits dispersive behavior. Then, the plasmonic mode returns the action (back action) on the vibrational oscillation, and this mechanism is especially favorable when the laser energy is blue-shifted from the plasmon cavity resonance energy. The back-action mechanism then pointed out the parametric amplification that could increase the SERS enhancement intensity [2,64,65].

If we assume that there are small protuberances (smaller than spheres of 2 nm), the excitation laser energy satisfies the blue shift condition (Fig. 13(a) and Fig. S7). Thus, the dynamic back-action mechanism could successfully explain the high SERS intensity observed in our experiments.

The fluctuation phenomena could have occurred because of the spontaneous and stochastic formation and destruction of these protuberances. This could occur because the experiments were conducted at room temperature (300 K). In other words, the protuberances could be formed by local thermal fluctuations on the Au nanocylinder surface [56,57,62]. In our results, the fluctuation exhibited more stochastic behavior when the laser power was decreased. Therefore, the random protuberance formation and destruction were almost independent of the laser power. Furthermore, the dynamic back-action mechanism explained the low SERS intensities when the excitation laser sources were 633 nm and 532 nm.

This is because these energies are very distant (blueshift) from the plasmon cavity peak (796 nm), but the 785 nm laser is close to the plasmon peak. The latter case is the desired condition for efficient dynamic back action and enhancement of Stokes Raman spectroscopy. This occurs because the best condition occurs when the laser is blue-shifted from the plasmon cavity peak in $\Delta = \omega_L - \omega_C = \omega_m$, where ω_m corresponds to the angular frequency of the molecular vibrational mode. As in our sample, the Raman Stokes lines were in the region of the plasmon cavity band (theoretically predicted for small bumps) when excited with a 785 nm laser, the necessary condition for a parametric intensification is given (Fig S7). The discussion above strongly suggests that the SERS fluctuations in our sample were due to the random formation and destruction of small bumps (picocavities), as also suggested by Wang and Rothberg, Carnegie et al., and Lindquist et al. [56,57,62]. The SERS fluctuation may also depend on the molecular diffusion [62,66] and/or structural changes in molecules in the hot spot region (enhanced near-field region), as reported in [57,62].

The SERS fluctuations of NAD in the array of Au nanocylinders with a diameter of 60 nm were highly random over time. In addition, the vibrational frequencies did not show any persistent Raman lines. These fluctuations are very different from those reported in the literature. The literature reported the existence of persistent Raman lines with a blinking effect and some other Raman lines without changing their vibrational frequencies [56,57].

In our sample, the high SERS enhancement accompanied by strong random fluctuations in time suggests the possible random formation and random destruction of small protuberances on the Au nanocylinder surface. On the nanocylinder surface, these small bumps are responsible for the formation of picocavities, as indicated by the near-field calculation for these types of structures (Fig. 13). However, the strong fluctuation in the vibrational frequencies, together with the non-existence of persistent Raman lines, strongly suggests that NAD molecules are not adsorbed by a specific bond of the molecule. This behavior could not be explained by considering the formation and destruction of the picocavities. It is, therefore, necessary to consider the possible spatial and rotational movements of the molecule. The question is as follows: what forces can potentiate this type of movement in the NAD molecule? In the text that follows, we suggest a possible mechanism for the mechanical dynamics of NAD molecules on the Au nanoarray surface.

Note that the persistent Raman line is related to the vibrational mode belonging to the bond of molecules that stationarily bind to the surface of the Au nanoparticles. Thus, the fluctuation of the vibrational frequencies could be due to the mechanical movement of NAD molecules, as

Optical Materials EXPRESS

suggested in the above discussion. This movement occurs together with picocavity formation and/or destruction. The fluctuation in frequency was more pronounced at a low laser power. For this reason, the Brownian movement of NAD molecules may have a low contribution to the mode frequency fluctuations.

These results suggest that the mechanical movement (dislocation and/or rotation) could be due to the high gradient field intensity originating from the picocavities. This could be because the mechanical force exerted over the molecules near the center of the picocavities has a significant effect on promoting NAD mechanical movement. It has been reported that the mechanical potential energy for the molecules near the hot spot is proportional to the intensity of the electric field [Eq. (8)].

$$\langle U \rangle = -\frac{1}{4} Re(\alpha)|E|^2 \tag{8}$$

The gradient force is given as follows [Eq. (9)]:

$$\langle F \rangle = -\nabla \langle U \rangle = \frac{1}{2} Re(\alpha) \nabla |E|^2 \tag{9}$$

where α is the molecular polarizability of the molecules near the hot spot [67,68]. The equations Eq. (8) and Eq. (9) are valid only when the dimensions of the molecule are much smaller than the optical wavelength of the electric field (λ). In this study, we considered the effective diameter of a molecule as its spatial dimension. In our system, this condition was fully satisfied because NAD molecules have a spatial extension of a few tens of Å and the plasmon bumps were placed at λ = 796 nm. For a rough theoretical calculation of $\langle U \rangle$ and $\langle F \rangle$, we considered α = 13.1 Å^3, which is the adenine part polarizability of NAD [69] and a one-dimensional spatial (x) profile of $|E|^2$, which corresponds to the electric near field at 796 nm (plasmon cavity resonance) induced by a 2 nm spherical protuberance (see Fig. 13(a)). In this calculation, we also considered that the sample was excited with a laser power of 700 μW. The laser was focused on the 1 μm^2 area, producing a power of 700 $\mu W/\mu m^2$. The intensity at the hot spot was corrected by the fraction of the effective area occupied by the hot spots within the unitary cell. Thus, the Lumerical FDTD platform was used for near-field calculations, and the effective area was calculated using Eq. (10) and Eq. (11) [70].

$$A_{eff} = \frac{1}{Max[W(r)]} \int_{Unitary\ cell} W(r)\, dA \tag{10}$$

$$W(r) = \frac{1}{2} Re\left\{ \frac{d[\omega \varepsilon(r)]}{d\omega} \right\} |E|^2 + \frac{1}{2} \mu_0 |H|^2 \tag{11}$$

where W(r) is the electromagnetic density as a function of position, ε(r) is the electric permittivity of the medium, and ω is the angular frequency of the light signal. The fraction of the area occupied by the hot spots was $f = A_{eff}/A_{unitary\ cell} = 1.79 \times 10^{-2}$. The intensity field at the hot spot was thus considered as $f \times 700 \mu W/\mu m^2$. The results of these calculations are shown in Fig. 14.

The U/10K$_B$T curve showed a minimum value close to 3.3. This indicates that the |U| potential is 3.3 times greater than the 10 K $_B$T thermal energy at room temperature (300 K). This result reveals that the hot-spot electromagnetic energy surpassed the thermal energy. Therefore, any mechanical movement of molecules close to these hot spots could be dominated by the gradient force rather than Brownian motion. The red curve corresponds to the gradient force obtained from $\langle F \rangle = -\nabla \langle U \rangle$. The results revealed that the maximum force reached was 8.5 nN, which is greater than that reported in the literature. [67,68].

From the discussion above, we suggest that the high fluctuation of SERS over normal mode frequencies could be related to the action of the gradient force on NAD. The gradient force is induced by the random creation and destruction of picocavities. This force may displace or rotate

Optical Materials EXPRESS

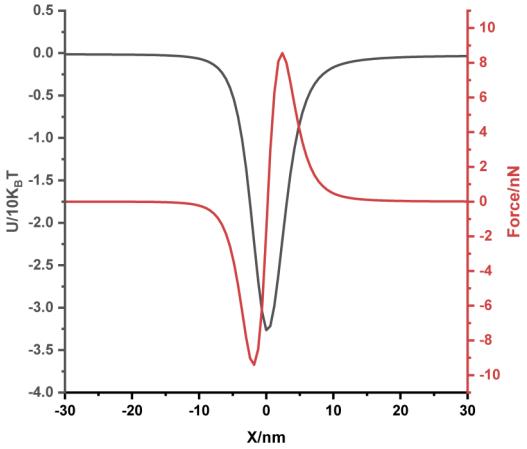

Fig. 14. Black line curve corresponds to the normalized potential energy of a NAD molecule induced by the electric field intensity of the hot spots generated by the bumps. The normalization was over 10 times the thermal energy at room temperature (300 K). The red curve corresponds to the gradient force experienced by NAD molecules near the hot spot region, which is given in nano Newtons.

NAD molecules, changing their configurations on the surface of the picocavities. Note that the fluctuation over the normal mode frequencies is still observed at a low laser power (70 nW). This event is expected only if the picocavities have dimensions less than those of the 2 nm bumps used for the theoretical discussion.

In summary, the SERS fluctuation event, in time and over normal mode frequencies, observed in the present study could be due to random picocavity generation over the nanocylinder surface. The hot spot from the picocavities induced gradient forces that changed the NAD configuration over the picocavities surface. Thus, the SERS fluctuations over the normal mode frequencies were promoted.

4. Conclusions

In this study, Au nanocylinder arrays were fabricated using a simple fabrication process using organized porous alumina structures as a mechanical mask. The nanocylinder arrays were formed after the deposition of Au using the electron beam technique. Scanning electron microscopy revealed a hexagonal organized array of Au nanocylinders. The array structure was also verified by reflectance spectroscopy. The array of Au nanocylinders with a diameter of 60 nm and periodicity of 126 nm was the best SERS surface. The efficient SERS surface of this sample is related to its fabrication process. For this surface, the Au deposition process was performed in two steps: first, 20 nm of Au was deposited by an electron beam; then, 2 nm of Au was deposited by sputtering. The other arrays were obtained by a one-step deposition process using an electron beam. A theoretical calculation also demonstrated that the array of Au nanocylinders with a diameter of 60 nm was the best SERS surface.

The extremely high SERS intensity of NAD on the SERS surface and fluctuation over time revealed a single-molecule SERS event. The detection of a single molecule was assumed because a monolayer of NAD was deposited on the SERS surface. The Raman line fluctuation was an uncorrelated event over time, especially when the power of the excitation laser was less than 700 μW. This was observed even with an exceptionally low power laser; the fluctuation event was still verified at 70 nW. The high SERS intensities and fluctuation events were discussed in terms of the dynamic back-action parametric interaction between the plasmon mode and vibrational modes.

Optical Materials EXPRESS

The FDTD calculation strongly suggested that the SERS enhancement on the best SERS surface was promoted by the dynamic back-action mechanism. Essentially, a high SERS enhancement occurs owing to the parametric coupling between the plasmon cavity and molecular vibration modes.

The experimental results suggest that the plasmon cavities originated from the spontaneous formation and destruction of small protuberances (less than 2 nm in size) on the nanocylinder surface. This induced a high near-field enhancement, as verified by theoretical calculations. In addition, the protuberance formation and destruction could have promoted the SERS fluctuation event over time, as also suggested in [57]. The fluctuation over normal mode frequencies was also related to the random formation/destruction of small cavities through gradient forces. These forces were induced by the high near-field enhancement in small cavities, as indicated bytheoretical calculations.

Funding. Coordenação de Aperfeiçoamento de Pessoal de Nível Superior (process number: 88882.333370/2019-01).

Acknowledgments. The authors would like to thank Ronaldo Domingues Mansano for providing optical analysis resources, Amber Hammond for text revision, and IFSP (Instituto Federal de Educação, Ciência e Tecnologia de São Paulo, Campus Cubatão) for its support.

Disclosures. The authors declare no conflicts of interest.

Data availability. No data were generated or analyzed in the presented research.

Supplemental document. See Supplement 1 for supporting content.

References

1. T. Itoh and Y. S. Yamamoto, "Between plasmonics and surface-enhanced resonant Raman spectroscopy: toward single-molecule strong coupling at a hotspot," Nanoscale **13**(3), 1566–1580 (2021).
2. Y. Zhang, R. Esteban, R. A. Boto, M. Urbieta, X. Arrieta, C. Shan, S. Li, J. J. Baumberg, and J. Aizpurua, "Addressing molecular optomechanical effects in nanocavity-enhanced Raman scattering beyond the single plasmonic mode," Nanoscale **13**(3), 1938–1954 (2021).
3. H. Lai, G. Li, F. Xu, and Z. Zhang, "Metal–organic frameworks: opportunities and challenges for surface-enhanced Raman scattering–a review," J. Mater. Chem. C **8**(9), 2952–2963 (2020).
4. P. A. Mosier-Boss, "Review of sers substrates for chemical sensing," Nanomaterials **7**(6), 142 (2017).
5. R. Pilot, R. Signorini, C. Durante, L. Orian, M. Bhamidipati, and L. Fabris, "A review on surface-enhanced Raman scattering," Biosensors **9**(2), 57 (2019).
6. M. Fan, G. F. Andrade, and A. G. Brolo, "A review on recent advances in the applications of surface-enhanced Raman scattering in analytical chemistry," Anal. Chim. Acta **1097**, 1–29 (2020).
7. U. Kreibig and M. Vollmer, *Optical Properties of Metal Clusters*, vol. 25 (Springer Science & Business Media, 2013).
8. S. A. Maier, *Plasmonics: Fundamentals and Applications* (Springer, 2007).
9. S. Link and M. A. El-Sayed, "Spectral properties and relaxation dynamics of surface plasmon electronic oscillations in gold and silver nanodots and nanorods," J. Phys. Chem. B **103**(40), 8410–8426 (1999).
10. R. Jin, Y. Cao, C. A. Mirkin, K. L. Kelly, G. C. Schatz, and J. Zheng, "Photoinduced conversion of silver nanospheres to nanoprisms," Science **294**(5548), 1901–1903 (2001).
11. R. Averitt, D. Sarkar, and N. Halas, "Plasmon resonance shifts of au-coated au 2 s nanoshells: insight into multicomponent nanoparticle growth," Phys. Rev. Lett. **78**(22), 4217–4220 (1997).
12. J. Aizpurua, P. Hanarp, D. Sutherland, M. Käll, G. W. Bryant, and F. G. De Abajo, "Optical properties of gold nanorings," Phys. Rev. Lett. **90**(5), 057401 (2003).
13. J. Aizpurua, G. W. Bryant, L. J. Richter, F. G. De Abajo, B. K. Kelley, and T. Mallouk, "Optical properties of coupled metallic nanorods for field-enhanced spectroscopy," Phys. Rev. B **71**(23), 235420 (2005).
14. A. M. Funston, C. Novo, T. J. Davis, and P. Mulvaney, "Plasmon coupling of gold nanorods at short distances and in different geometries," Nano Lett. **9**(4), 1651–1658 (2009).
15. F. Hao, C. L. Nehl, J. H. Hafner, and P. Nordlander, "Plasmon resonances of a gold nanostar," Nano Lett. **7**(3), 729–732 (2007).
16. S. M. Novikov, A. Sánchez-Iglesias, M. K. Schmidt, A. Chuvilin, J. Aizpurua, M. Grzelczak, and L. M. Liz-Marzán, "Gold spiky nanodumbbells: Anisotropy in gold nanostars," Part. Part. Syst. Charact. **31**(1), 77–80 (2014).
17. K.-H. Su, Q.-H. Wei, X. Zhang, J. Mock, D. R. Smith, and S. Schultz, "Interparticle coupling effects on plasmon resonances of nanogold particles," Nano Lett. **3**(8), 1087–1090 (2003).
18. W. Rechberger, A. Hohenau, A. Leitner, J. Krenn, B. Lamprecht, and F. Aussenegg, "Optical properties of two interacting gold nanoparticles," Opt. Commun. **220**(1-3), 137–141 (2003).
19. J. A. Fan, C. Wu, K. Bao, J. Bao, R. Bardhan, N. J. Halas, V. N. Manoharan, P. Nordlander, G. Shvets, and F. Capasso, "Self-assembled plasmonic nanoparticle clusters," Science **328**(5982), 1135–1138 (2010).

Optical Materials EXPRESS

20. A. Yanai, M. Grajower, G. M. Lerman, M. Hentschel, H. Giessen, and U. Levy, "Near-and far-field properties of plasmonic oligomers under radially and azimuthally polarized light excitation," ACS Nano **8**(5), 4969–4974 (2014).
21. X. Xiu, L. Hou, J. Yu, S. Jiang, C. Li, X. Zhao, Q. Peng, S. Qiu, C. Zhang, B. Man, and Z. Li, "Manipulating the surface-enhanced Raman spectroscopy (sers) activity and plasmon-driven catalytic efficiency by the control of ag np/graphene layers under optical excitation," Nanophotonics **10**(5), 1529–1540 (2021).
22. C. Li, S. Xu, J. Yu, Z. Li, W. Li, J. Wang, A. Liu, B. Man, S. Yang, and C. Zhang, "Local hot charge density regulation: Vibration-free pyroelectric nanogenerator for effectively enhancing catalysis and in-situ surface enhanced Raman scattering monitoring," Nano Energy **81**, 105585 (2021).
23. W.-H. Park, S.-H. Ahn, and Z. H. Kim, "Surface-enhanced Raman scattering from a single nanoparticle–plane junction," ChemPhysChem **9**(17), 2491–2494 (2008).
24. L. Rodriguez-Lorenzo, R. A. Alvarez-Puebla, F. J. G. de Abajo, and L. M. Liz-Marzán, "Surface enhanced Raman scattering using star-shaped gold colloidal nanoparticles," J. Phys. Chem. C **114**(16), 7336–7340 (2010).
25. M. D. Sonntag, E. A. Pozzi, N. Jiang, M. C. Hersam, and R. P. Van Duyne, "Recent advances in tip-enhanced Raman spectroscopy," J. Phys. Chem. Lett. **5**(18), 3125–3130 (2014).
26. A. Lombardi, A. Demetriadou, L. Weller, P. Andrae, F. Benz, R. Chikkaraddy, J. Aizpurua, and J. J. Baumberg, "Anomalous spectral shift of near-and far-field plasmonic resonances in nanogaps," ACS Photonics **3**(3), 471–477 (2016).
27. P. G. Etchegoin, M. Meyer, and E. Le Ru, "Statistics of single molecule sers signals: is there a poisson distribution of intensities?" Phys. Chem. Chem. Phys. **9**(23), 3006–3010 (2007).
28. T. Brule, A. Bouhelier, H. Yockell-Lelievre, J.-E. Clement, A. Leray, A. Dereux, and E. Finot, "Statistical and fourier analysis for in-line concentration sensitivity in single molecule dynamic-sers," ACS Photonics **2**(9), 1266–1271 (2015).
29. M. Barbry, P. Koval, F. Marchesin, R. Esteban, A. G. Borisov, J. Aizpurua, and D. Sánchez-Portal, "Atomistic near-field nanoplasmonics: reaching atomic-scale resolution in nanooptics," Nano Lett. **15**(5), 3410–3419 (2015).
30. T. Itoh and Y. S. Yamamoto, "Recent topics on single-molecule fluctuation analysis using blinking in surface-enhanced resonance Raman scattering: clarification by the electromagnetic mechanism," Analyst **141**(17), 5000–5009 (2016).
31. M. G. Rossmann, "Molecular structure of nad," Nature **262**(5570), 726 (1976).
32. M. J. MacDonald and L. K. Marshall, "Mouse lacking nad+-linked glycerol phosphate dehydrogenase has normal pancreatic beta cell function but abnormal metabolite pattern in skeletal muscle," Arch. Biochem. Biophys. **384**(1), 143–153 (2000).
33. L. A. Sanni, C. Rae, A. Maitland, R. Stocker, and N. H. Hunt, "Is ischemia involved in the pathogenesis of murine cerebral malaria?" Am. J. Pathol. **159**(3), 1105–1112 (2001).
34. P. D. Mongan, J. Capacchione, S. West, J. Karaian, D. Dubois, R. Keneally, and P. Sharma, "Pyruvate improves redox status and decreases indicators of hepatic apoptosis during hemorrhagic shock in swine," American Journal of Physiology-Heart and Circulatory Physiology (2002).
35. A. Gaikwad, D. J. Long II, J. L. Stringer, and A. K. Jaiswal, "In vivo role of nad (p) h: quinone oxidoreductase 1 (nqo1) in the regulation of intracellular redox state and accumulation of abdominal adipose tissue," J. Biol. Chem. **276**(25), 22559–22564 (2001).
36. P. Belenky, K. L. Bogan, and C. Brenner, "Nad+ metabolism in health and disease," Trends Biochem. Sci. **32**(1), 12–19 (2007).
37. V. Schreiber, F. Dantzer, J.-C. Ame, and G. De Murcia, "Poly (adp-ribose): novel functions for an old molecule," Nat. Rev. Mol. Cell Biol. **7**(7), 517–528 (2006).
38. R. M. Anderson, K. J. Bitterman, J. G. Wood, O. Medvedik, H. Cohen, S. S. Lin, J. K. Manchester, J. I. Gordon, and D. A. Sinclair, "Manipulation of a nuclear nad+ salvage pathway delays aging without altering steady-state nad+ levels," J. Biol. Chem. **277**(21), 18881–18890 (2002).
39. A. Katoh and T. Hashimoto, "Molecular biology of pyridine nucleotide and nicotine biosynthesis," Front Biosci. **9**(1-3), 1577–1586 (2004).
40. N. Pollak, C. Dölle, and M. Ziegler, "The power to reduce: pyridine nucleotides–small molecules with a multitude of functions," Biochem. J. **402**(2), 205–218 (2007).
41. A. H. Guse, "Calcium mobilizing second messengers derived from nad," Biochim. Biophys. Acta, Proteins Proteomics **1854**(9), 1132–1137 (2015).
42. H. C. Lee, "Cyclic adp-ribose and nicotinic acid adenine dinucleotide phosphate (naadp) as messengers for calcium mobilization," J. Biol. Chem. **287**(38), 31633–31640 (2012).
43. F. Aredia and A. I. Scovassi, "Poly (adp-ribose): a signaling molecule in different paradigms of cell death," Biochem. Pharmacol. **92**(1), 157–163 (2014).
44. M. M. Rosado, E. Bennici, F. Novelli, and C. Pioli, "Beyond dna repair, the immunological role of parp-1 and its siblings," Immunology **139**(4), 428–437 (2013).
45. L. Durnin, Y. Dai, I. Aiba, C. W. Shuttleworth, I. A. Yamboliev, and V. N. Mutafova-Yambolieva, "Release, neuronal effects and removal of extracellular β-nicotinamide adenine dinucleotide (β-nad+) in the rat brain," Eur. J. Neurosci. **35**(3), 423–435 (2012).
46. H. Yang, T. Yang, J. A. Baur, E. Perez, T. Matsui, J. J. Carmona, D. W. W. Lamming, N. C. Souza-Pinto, V. A. Bohr, A. Rosenzweig, R. de Cabo, A. A. A. Sauve, and D. A. Sinclair, "Nutrient-sensitive mitochondrial nad+ levels dictate cell survival," Cell **130**(6), 1095–1107 (2007).

Optical Materials EXPRESS

47. K. Pankiewicz, R. Petrelli, R. Singh, and K. Felczak, "Nicotinamide adenine dinucleotide based therapeutics, update," Curr. Med. Chem. **22**(34), 3991–4028 (2015).
48. A. Woźniacka, A. Sysa-Jędrzejowska, J. Adamus, and J. Gębicki, "Topical application of NADH for the treatment of rosacea and contact dermatitis," Clin. Exp. Dermatol. Clin. cases **28**(1), 61–63 (2003).
49. N. Braidy, R. Grant, and P. S. Sachdev, "Nicotinamide adenine dinucleotide and its related precursors for the treatment of alzheimer's disease," Curr. opinion psychiatry **31**(2), 160–166 (2018).
50. Y.-J. Xiao, Y.-F. Chen, and X.-X. Gao, "Comparative study of the surface enhanced near infrared Raman spectra of adenine and nad+ on a gold electrode," Spectrochim. Acta, Part A **55**(6), 1209–1218 (1999).
51. H. Yang, Z. Zhang, G. Shen, and R. Yu, "In situ Raman spectra of an NAD+-modified silver electrode at various potentials," J. Raman Spectrosc. **35**(3), 190–194 (2004).
52. H. Yang, Y. Yang, Z. Liu, Z. Zhang, G. Shen, and R. Yu, "Self-assembled monolayer of nad at silver surface: a Raman mapping study," Surf. Sci. **551**(1-2), 1–8 (2004).
53. K. T. Yue, C. L. Martin, D. Chen, P. Nelson, D. L. Sloan, and R. Callender, "Raman spectroscopy of oxidized and reduced nicotinamide adenine dinucleotides," Biochemistry **25**(17), 4941–4947 (1986).
54. S. Ramalingam, S. Periandy, M. Govindarajan, and S. Mohan, "Ft-ir and ft-Raman vibrational spectra and molecular structure investigation of nicotinamide: a combined experimental and theoretical study," Spectrochim. Acta, Part A **75**(5), 1552–1558 (2010).
55. P. Alonso-González, P. Albella, M. Schnell, J. Chen, F. Huth, A. García-Etxarri, F. Casanova, F. Golmar, L. Arzubiaga, L. Hueso, J. Aizpurua, and R. Hillenbrand, "Resolving the electromagnetic mechanism of surface-enhanced light scattering at single hot spots," Nat. Commun. **3**(1), 684 (2012).
56. Z. Wang and L. J. Rothberg, "Origins of blinking in single-molecule Raman spectroscopy," J. Phys. Chem. B **109**(8), 3387–3391 (2005).
57. C. Carnegie, J. Griffiths, B. de Nijs, C. Readman, R. Chikkaraddy, W. M. Deacon, Y. Zhang, I. Szabo, E. Rosta, J. Aizpurua, and J. J. Baumberg, "Room-temperature optical picocavities below 1 nm^3 accessing single-atom geometries," J. Phys. Chem. Lett. **9**(24), 7146–7151 (2018).
58. F. Benz, M. K. Schmidt, A. Dreismann, R. Chikkaraddy, Y. Zhang, A. Demetriadou, C. Carnegie, H. Ohadi, B. De Nijs, R. Esteban, J. Aizpurua, and J. J. Baumberg, "Single-molecule optomechanics in picocavities," Science **354**(6313), 726–729 (2016).
59. R. M. Haralick, K. Shanmugam, and I. H. Dinstein, "Textural features for image classification," IEEE Trans. Syst., Man, Cybern. **SMC-3**(6), 610–621 (1973).
60. Y. Park and J.-M. Guldmann, "Measuring continuous landscape patterns with gray-level co-occurrence matrix (GLCM) indices: An alternative to patch metrics?" Ecol. Indic. **109**, 105802 (2020).
61. A. Eleyan and H. Demirel, "Co-occurrence matrix and its statistical features as a new approach for face recognition," Turkish J. Electr. Eng. & Comput. Sci. **19**(1), 97–107 (2011).
62. N. C. Lindquist, C. D. L. de Albuquerque, R. G. Sobral-Filho, I. Paci, and A. G. Brolo, "High-speed imaging of surface-enhanced Raman scattering fluctuations from individual nanoparticles," Nat. Nanotechnol. **14**(10), 981–987 (2019).
63. M. Aspelmeyer, T. J. Kippenberg, and F. Marquardt, "Cavity optomechanics," Rev. Mod. Phys. **86**(4), 1391–1452 (2014).
64. M. K. Schmidt, R. Esteban, A. González-Tudela, G. Giedke, and J. Aizpurua, "Quantum mechanical description of Raman scattering from molecules in plasmonic cavities," ACS Nano **10**(6), 6291–6298 (2016).
65. P. Roelli, C. Galland, N. Piro, and T. J. Kippenberg, "Molecular cavity optomechanics as a theory of plasmon-enhanced Raman scattering," Nat. Nanotechnol. **11**(2), 164–169 (2016).
66. K.-D. Park, E. A. Muller, V. Kravtsov, P. M. Sass, J. Dreyer, J. M. Atkin, and M. B. Raschke, "Variable-temperature tip-enhanced Raman spectroscopy of single-molecule fluctuations and dynamics," Nano Lett. **16**(1), 479–487 (2016).
67. A. N. Koya, J. Cunha, T.-L. Guo, A. Toma, D. Garoli, T. Wang, S. Juodkazis, D. Cojoc, and R. Proietti Zaccaria, "Novel plasmonic nanocavities for optical trapping-assisted biosensing applications," Adv. Opt. Mater. **8**(7), 1901481 (2020).
68. P. C. Ke and M. Gu, "Characterization of trapping force on metallic Mie particles," Appl. Opt. **38**(1), 160–167 (1999).
69. M. Gussoni, M. Rui, and G. Zerbi, "Electronic and relaxation contribution to linear molecular polarizability: an analysis of the experimental values," J. Mol. Struct. **447**(3), 163–215 (1998).
70. X. Zhang, W. J. Salcedo, M. M. Rahman, and A. G. Brolo, "Surface-enhanced Raman scattering from bowtie nanoaperture arrays," J. Surf. Sci. **676**, 39–45 (2018).